

Article

Theoretical Study on Spin-Selective Coherent Electron Transfer in a Quantum Dot Array

Shumpei Masuda ^{1,*} , Kuan Yen Tan ^{2,3}  and Mikio Nakahara ⁴ ¹ College of Liberal Arts and Sciences, Tokyo Medical and Dental University, Ichikawa 272-0827, Japan² QCD Labs, QTF Center of Excellence, Department of Applied Physics, Aalto University, 00076 Aalto, Finland; kuan.tan@aalto.fi³ IQM Finland Oy, Vaisalanatie 6 C, 02130 Espoo, Finland⁴ Department of Mathematics, Shanghai University, 99 Shangda Road, Shanghai 200444, China; nakahara@shu.edu.cn

* Correspondence: masulas@tmd.ac.jp

Received: 17 October 2019; Accepted: 17 December 2019; Published: 22 December 2019

Abstract: Recently, we proposed the spin-selective coherent electron transfer in a silicon-quantum-dot array. It requires temporal tuning of two pulses of an oscillating magnetic field and gate voltage control. This paper proposes a simpler method that requires a single pulse of oscillating magnetic field and gate voltage control. We examined the robustness of the control against the error in the pulse amplitude and the effect of the excited states relaxation to the control efficiency. In addition, we propose a novel control method based on a shortcuts-to-adiabaticity protocol, which utilizes two pulses but requires temporal control of the pulse amplitude for only one of them. We compared their efficiencies under the effect of realistic pulse amplitude errors and relaxation.

Keywords: spin-selective electron transfer; STIRAP; shortcuts to adiabaticity

1. Introduction

Spins in silicon-based quantum dots are a promising candidate for fault-tolerant quantum information processing (QIP) [1]. Readout and single-qubit gate control fidelities above the surface code threshold [2] have been experimentally demonstrated by taking advantage of exceptionally long longitudinal relaxation times [3–5] and transverse relaxation times [6–9]. These are two figures of merit that are highly desirable for a scalable quantum computer. High fidelity spin readout has been demonstrated in a CMOS device by its robustness with respect to temperature [10]. Recently, high-fidelity single qubit operations above 1 K have also been demonstrated, potentially reducing large-scale quantum processor design constraints [11]. It is known that all single-qubit gates, and one of two-qubit gates that entangles two qubits, such as the CNOT gate, form the universal set of gates. Entanglement can be introduced only by a non-local operation, such as the one introduced in [12]. Several types of quantum gate operations, including two-qubit quantum gates, have been demonstrated [13–15] by employing the exchange interaction between single spins in isotopically enriched silicon [16]. Furthermore, single electron pumps [17–23] and shuttling of single electron [24,25] in quantum dot array have been also demonstrated at the level of metrological accuracy. The coherent spin displacement of individual electrons has been demonstrated in a GaAs system quantum dot array [26].

Inspired by a theoretical analysis of two-qubit gate implementation employing state-dependent potentials in cold atom systems in optical fiber array [27–29], we recently proposed a spin-selective electron transfer method described in [12], which realizes non-local qubit operations in a quantum dot array. This proposal also offers quantum non-demolition measurement of electron spin [30–32] provided that the electron position is measured without introducing the dissipation to the electron.

Quantum non-demolition measurements can be used for improvement of qubit operations. In our previous method, temporal tuning of two pulses of an oscillating magnetic field was required.

In this paper, we report a simplified and improved method of spin-selective coherent electron transfer in a silicon-quantum-dot array driven by a single pulse of oscillating magnetic field and gate voltage control. We examine the robustness of the control against the pulse amplitude error and the effect of the relaxation to control efficiency. We also propose a method based on the shortcut-to-adiabaticity (STA) protocol, which utilizes two pulses but requires temporal control of one of the pulses only.

We present the framework of the spin-selective electron transfer with a single π -pulse in Section 2, and the adiabatic and the shortcuts-to-adiabaticity controls in Section 3. In Section 4, we compare the robustness of the controls against the pulse amplitude error, the relaxation of excited states and the dephasing of a spin.

2. Spin-Selective Electron Transfer with a Single π -Pulse

Figure 1a schematically shows the system under consideration, where two-dimensional electron gas is in the yz -plane. A stretched quantum dot (Dot 0) is located along the z -axis. We assume that the confinement of the electron in the y direction is at least twice tighter than the confinement in the z direction. Thus, the one-dimensional model can approximate a few of the lowest-energy eigenstates of the dot that we utilize. There is a time-independent uniform magnetic field $\mathbf{B}_z = (0, 0, B_z)$ along the z -axis. A conducting lead (blue line) carries the AC current, I_p , which produces the pump magnetic field $\mathbf{B}_p = (B_p, 0, 0)$ along the x -axis perpendicular to the two-dimensional electron gas. The conducting lead is separated from the center of Dot 0 by distance r_0 , and is tilted with respect to the z -axis by angle θ_0 to introduce the spatial inhomogeneity of B_p in Dot 0 [12], which is essential for our proposal, as shown in Equation (4). We assume that the initial condition of the electron trapped in Dot 0 is a superposition of the spin-up ground state and the spin-down ground state. The squared amplitudes of the wave functions of the three low-lying eigenstates for either spin-up or spin-down are shown in Figure 1b.

Our spin-selective electron transfer protocol is illustrated in Figure 1c. The protocol is composed of two steps. In Step I the lowest energy spin-down state is transferred to the first spin-up excited state, while the lowest energy spin-up state is left unchanged. In Step II the center potential barrier is adiabatically raised to split Dot 0 into two potential wells: Dot 1 and Dot 2. The depths of the potential wells are tuned so that the bottom of the potential of Dot 2 becomes above that of Dot 1. As the potential is modified, the wave function of the first spin-up excited state is carried into Dot 2 because the wave function of the instantaneous first excited eigenstate with spin-up is mostly located in Dot 2. The wave function of the lowest energy spin-up state is loaded into Dot 1. Two states are individually accessible after the wave function is separated into two Dots. Thus, it can be used for non-local multi-qubit operation when this scheme is applied to a multi-electron system [12].

Previously, we used another separate dot (Dot 4 in [12]) for Step I to avoid the possible fluctuation of the separation of the energy levels, which may be caused by the fluctuation of the gate voltages of the dots [12]. However, in this paper we do not employ such a separate dot in order to make the scheme simpler by assuming that the fluctuation of the gate voltages is negligible.

2.1. Step I

The electron is initially confined in Dot 0. We use the energy eigenstates of Dot 0 with $B_p = 0$ as the basis vectors of the system to explain the schemes of Step I. Figure 1d depicts the energy diagram of Dot 0. Here, $|i, \downarrow (\uparrow)\rangle$ for $i = 1, 2$ and 3 denotes the first three low-lying energy levels with spin-down (up) along the z direction. The separations of the adjacent energy eigenvalues are nonuniform due to the anharmonicity of the potential of the dot. The stationary magnetic field \mathbf{B}_z causes the Zeeman splitting with energy difference $g\mu_B B_z/\hbar$ between the spin-up and down states, where g is the electron g -factor and μ_B is the Bohr magneton.

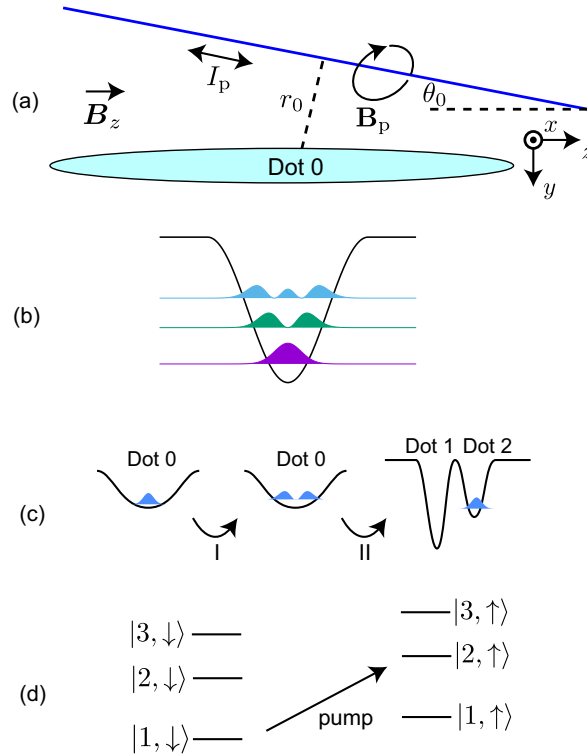


Figure 1. (a) Proposed system. The blue line represents the conducting lead carrying the AC control current I_p producing the magnetic field (pump field) $\mathbf{B}_p = (B_p, 0, 0)$ perpendicular to the surface. The conducting lead is tilted with respect to the z -axis by angle θ_0 . Here, r_0 is the distance of the lead from the center of Dot 0. The generated AC magnetic field couples the ground state and the first excited state in the dot. (b) Colors show the square of the amplitude of the wave functions of the three lowest eigenstates with either spin-up or spin-down in Dot 0. The black curve is the schematic of the potential of Dot 0. (c) Schematics of the spin-selective electron transfer. The black curves depict the potential profile of quantum dot(s) at each step. The blue color represents the squared amplitude of the wave function of an electron whose initial spin was down. (d) Energy diagram of the system in Step I. Here, $|i, \uparrow (\downarrow)\rangle$ is the i th instantaneous eigenstate of Dot 0 with spin-up (down). The pump field \mathbf{B}_p couples $|1, \downarrow\rangle$ and $|2, \uparrow\rangle$.

We aim at a spin-selective state transfer in which only the lowest energy spin-down electron is transferred from $|1, \downarrow\rangle$ to $|2, \uparrow\rangle$, while the lowest energy spin-up electron remains unaffected. The frequency ω_p of the pump field \mathbf{B}_p is adjusted to $\omega_p = (E_{2, \uparrow} - E_{1, \downarrow})/\hbar$, where $E_{i, \uparrow (\downarrow)}$ is the energy eigenvalue of $|i, \uparrow (\downarrow)\rangle$, so that \mathbf{B}_p couples $|1, \downarrow\rangle$ and $|2, \uparrow\rangle$. Note that $|1, \uparrow\rangle$ is not coupled to any states by \mathbf{B}_p . A typical value of $\omega_p/2\pi$ was calculated as 47 GHz in [12].

We consider the dynamics of a state which is in $|1, \downarrow\rangle$ at the initial time. The effective Hamiltonian of the system is written in terms of the subset $\{|1, \downarrow\rangle, |2, \uparrow\rangle\}$ of the states as a basis. The pulsed pump field \mathbf{B}_p employed in Step I is represented as

$$B_p(t, \mathbf{r}) = B_p^{(e)}(t)\eta(\mathbf{r})\cos(\omega_p t) \quad (1)$$

with the envelope function $B_p^{(e)}(t)$ of the pump field at the center of Dot 0. The function $\eta(\mathbf{r})$ is defined as the ratio of the intensity of the field at \mathbf{r} to $B_p^{(e)}$. In other words, $\eta(\mathbf{r})$ characterizes the spatial dependence of the pump magnetic field. The Hamiltonian of the two-level system can be written, by using the rotating frame and the rotating wave approximation (RWA), as

$$H_{\text{RWA}}(t) = \frac{\hbar}{2} \begin{pmatrix} 0 & \Omega_p(t) \\ \Omega_p(t) & 0 \end{pmatrix}, \quad (2)$$

with the Rabi frequency given by

$$\Omega_p(t) = \frac{B_p^{(e)}(t)g\mu_B\mu_p}{2\hbar}, \quad (3)$$

and the overlapping factor defined by

$$\mu_p = \int d\mathbf{r}\phi_1(\mathbf{r})\eta(\mathbf{r})\phi_2(\mathbf{r}), \quad (4)$$

where $\phi_i(\mathbf{r}) = \langle \mathbf{r}, \downarrow (\uparrow) | i, \downarrow (\uparrow) \rangle$ (see Appendix A of [12] for the derivation of H_{RWA}). If the pump magnetic field \mathbf{B}_p were spatially uniform, μ_p would vanish because of the orthogonality of the energy eigenvectors with different eigenvalues and no coupling between the two eigenstates would be introduced. Thus, the nonuniformity $\eta(\mathbf{r})$ of the magnetic field is essential to couple the energy eigenstates.

We take the envelope function $B_p^{(e)}$ as

$$B_p^{(e)}(t) = \begin{cases} B_p^0 & \text{for } 0 \leq t \leq T_{\text{stepI}}, \\ 0 & \text{for } t < 0 \text{ and } t > T_{\text{stepI}}, \end{cases} \quad (5)$$

where B_p^0 is the rectangular pulse height and T_{stepI} is the pulse width, which defines the duration of Step I. When the pulse area is π , that is,

$$B_p^0 = \frac{2\pi\hbar}{g\mu_B\mu_p T_{\text{stepI}}}, \quad (6)$$

the state is transferred from $|1, \downarrow\rangle$ to $|2, \uparrow\rangle$ under the action of the pump pulse. Typical dynamics of the system are shown for $\mu_p = -0.05$ in Figure 2.

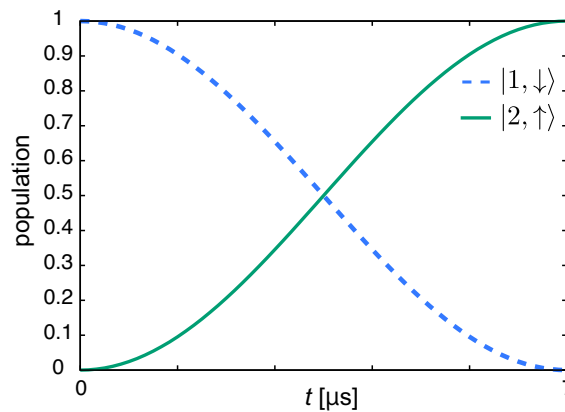


Figure 2. Time dependence of the populations for $\mu_p = -0.05$, $B_p^0 = 0.1$ mT and $T_{\text{stepI}} = 7$ μs .

2.2. Step II

As the middle potential barrier, which divides Dot 0 into Dot 1 and Dot 2, is raised, and the potential depth of Dot 2 is tuned, the wave functions of the ground and the first excited states are transferred into Dot 1 and Dot 2, respectively. We use the one-dimensional model with the rectangular potentials illustrated in Figure 3a to simulate Step II. The potentials for dots are approximated by the rectangular ones for simplicity. Details of the potential profile do not affect the result because this step employs adiabatic dynamics. V_{b_i} for $i = 1, 2, 3$ and V_{d_j} for $j = 1, 2$ denote the barrier heights and the potential depths of the dots, respectively. The widths of the dots L_d and the widths of the barriers L_b are all taken as 30 nm. At the initial time ($t = T_{\text{stepI}}$) of Step II, we take $V_{b2} = V_{d_j(=1,2)} = 0 < V_{b1} = V_{b3}$

so that the two dots are combined to form a single larger dot (Dot 0). The middle barrier height V_{b2} and the dot potential depth V_{d2} are adiabatically ramped from 0 to $V_{b2}^{(0)}$ and $V_{d2}^{(0)}$, respectively, as

$$V_{b2,d2} = V_{b2,d2}^{(0)}[R(t - T_{\text{stepI}})], \quad T_{\text{stepI}} \leq t \leq T_{\text{stepI}} + T_{\text{stepII}} \quad (7)$$

with $R(t) = [t - \sin(\omega_2 t)/\omega_2]/T_{\text{stepII}}$ and $\omega_2 = 2\pi/T_{\text{stepII}}$, while the other parameters are kept constant; $V_{b1,b3} = V_{b1,b3}^{(0)}$ and $V_{d1} = 0$, where T_{stepII} is the time required for Step II. R interpolates between 0 and 1 smoothly with $R(0) = 0$, $R(T_{\text{stepII}}) = 1$ and $R'(0) = R'(T_{\text{stepII}}) = 0$, where prime denotes the time derivative. Figure 3b depicts the time-evolution of the squared amplitude of the wave function whose initial state was $|1, \uparrow\rangle$, the spin-up ground state in Dot 0 with $T_{\text{stepII}} = 0.26$ ns. The wave function is transferred to Dot 1 and is mostly localized within Dot 1 at $t = T_{\text{stepI}} + T_{\text{stepII}}$. Figure 3c depicts the time-evolution of the squared amplitude of the wave function with the initial state $|2, \uparrow\rangle$. The wave function is transferred to Dot 2 and is mostly localized within Dot 2 at $t = T_{\text{stepI}} + T_{\text{stepII}}$. The fidelity of Step II, defined by the overlap between the state at $t = T_{\text{stepI}} + T_{\text{stepII}}$ and the target energy eigenstate, is more than 0.9999 for $T_{\text{stepII}} > 0.26$ ns. This shows that undesirable non-adiabatic transitions are safely negligible.

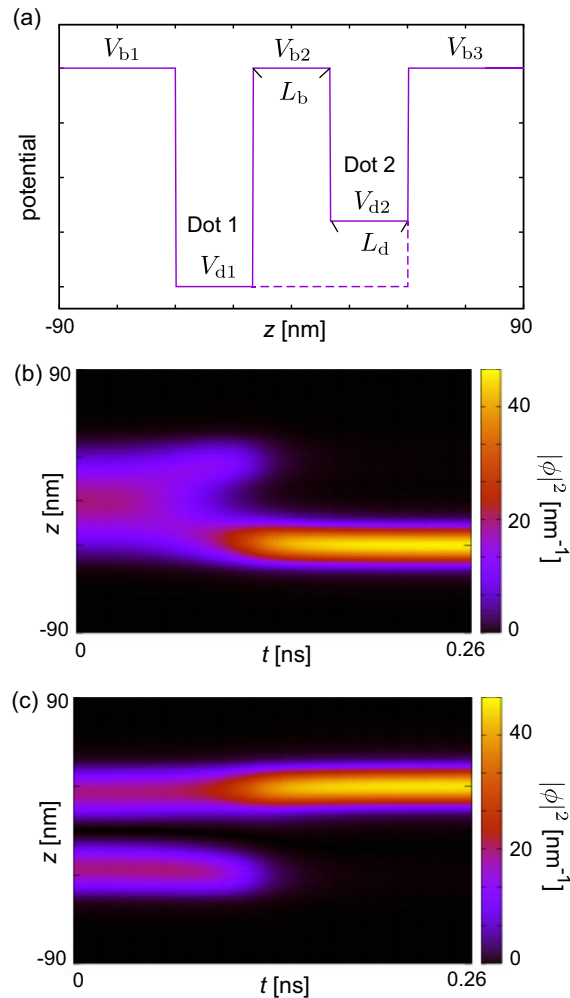


Figure 3. (a) Schematics of Dot 1 and Dot 2 in a one-dimensional model. V_{bi} and V_{dj} are the heights of the potential barriers and the depths of the potential wells, respectively. In this panel the difference in V_{dj} is exaggerated for purpose of illustration. The dashed line shows the potential profile at $t = T_{\text{stepI}}$. The time-evolution of the squared amplitude of the wave functions with initial states $|1, \uparrow\rangle$ (b) and $|2, \uparrow\rangle$ (c). The parameter set used was $L_d = L_b = 30$ nm, $V_{d1}^{(0)} = 0$, $V_{d2}^{(0)} = 179$ μ eV and $V_{bi}^{(0)} = 3.6$ meV.

3. Adiabatic and Shortcuts-To-Adiabaticity Controls

In this paper, we propose new improved protocols for Step I, which involves three states; namely, $|1, \downarrow\rangle$, $|2, \uparrow\rangle$ and $|3, \downarrow\rangle$ of Dot 0. The pump field B_p couples $|1, \downarrow\rangle$ and $|2, \uparrow\rangle$ while the Stokes field B_S couples $|2, \uparrow\rangle$ and $|3, \downarrow\rangle$. In contrast with the previous study [12], the envelope function of the Stokes field is kept constant in this work. Thus, the time-dependent tuning is required only for the pump field.

The schematic of our protocol is illustrated in Figure 4a. In Step I the lowest-energy spin-down state is transferred to the spin-down second excited state, while the lowest-energy spin-up state is left unaffected. Figure 4b shows the energy diagram relevant to Step I. In Step II the potential barriers are adiabatically raised to split Dot 0 to three potential wells: Dots 1, 2 and 3. The depths of the potential wells are tuned so that Dot 1 and Dot 3 have the lowest and the highest potential minima, respectively. The wave function of the second spin-down excited state is carried into Dot 3 because the wave function of the instantaneous second excited eigenstate with spin-down is located in Dot 3. On the other hand, the wave function of the lowest energy spin-up state is loaded to Dot 1. In the following, we mainly discuss Step I. See [12] for the numerical simulation for Step II.

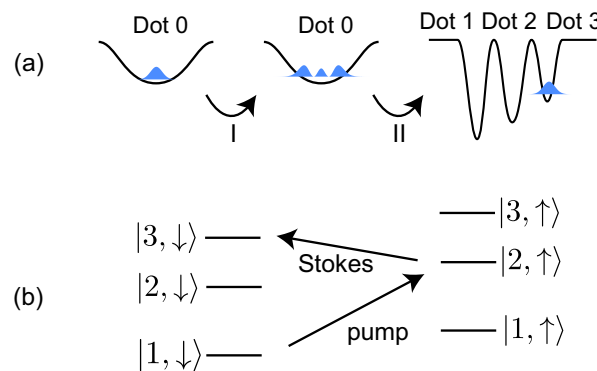


Figure 4. (a) Schematic description of the spin-selective single electron transfer. The black curves show the potential profiles of the quantum dot(s). The blue color represents the squared amplitude of the wave function of an electron whose initial spin was down. (b) Energy diagram of the system in Step I. The AC magnetic field B_p (pump field) couples $|1, \downarrow\rangle$ and $|2, \uparrow\rangle$, while B_S (Stokes field) couples $|2, \uparrow\rangle$ and $|3, \downarrow\rangle$.

We consider the dynamics of the state which is initially $|1, \downarrow\rangle$. A subset of states, $\{|1, \downarrow\rangle, |2, \uparrow\rangle, |3, \downarrow\rangle\}$, is used as the basis. We employ the rotating frame and the RWA to rewrite the Hamiltonian of the three-level system in the form

$$H_{\text{RWA}}(t) = \frac{\hbar}{2} \begin{pmatrix} 0 & \Omega_p(t) & 0 \\ \Omega_p(t) & 0 & \Omega_S \\ 0 & \Omega_S & 0 \end{pmatrix}, \quad (8)$$

with the Rabi frequencies Ω_p in Equation (3) and Ω_S given by

$$\Omega_S = \frac{B_S^{(e)} g \mu_B \mu_S}{2\hbar}, \quad (9)$$

and the overlapping factors defined by

$$\mu_S = \int dr \phi_2(\mathbf{r}) \eta(\mathbf{r}) \phi_3(\mathbf{r}). \quad (10)$$

We use $\mu_S = -0.078$ in this study. (See Appendix A of [12] for the derivation of H_{RWA}). We assume that Ω_p and Ω_S in Equation (8) can be controlled individually using two tone pulses. Typical frequencies of the pump and the Stokes fields are 47 GHz and 32 GHz, respectively [12].

3.1. Spin-Selective STIRAP with Constant $B_S^{(e)}$

We examine a protocol with a linearly increased pump field having recourse to the adiabatic dynamics of the system. The protocol is called stimulated Raman adiabatic passage (STIRAP) [33–35]. STIRAP has been widely studied for adiabatic transport of electrons [36,37], single atoms [38–43] and BECs [44–47], and population transfer of molecules [48–55]. It has already been demonstrated in various areas, such as control of a superconducting qubit [56], chemical reaction dynamics [57], laser-induced cooling of atomic gases [58], light beams propagating in three evanescently-coupled optical waveguides [59–62] and sound propagation in sonic crystals [63]. This protocol can be applied to transfer qubits coherently over long distance in spin-based quantum computing architecture [64].

The envelope functions of the pump and the Stokes fields for $t \leq T_{\text{stepI}}$ are given by

$$\begin{aligned} B_p^{(e)}(t) &= \begin{cases} 0 & \text{for } t \leq 0, \\ B_p^0 t / T_{\text{stepI}} & \text{for } 0 \leq t \leq T_{\text{stepI}}, \end{cases} \\ B_S^{(e)}(t) &= B_S^0. \end{aligned} \quad (11)$$

A time-dependent, field-dressed eigenstate of the system is represented as

$$|\phi_0(t)\rangle = \cos \Theta(t) |1, \downarrow\rangle - \sin \Theta(t) |3, \downarrow\rangle, \quad (12)$$

where $\Theta(t)$ is given by

$$\tan \Theta(t) = \frac{\Omega_p(t)}{\Omega_S}. \quad (13)$$

We assume that the initial state is $|1, \downarrow\rangle$ which is equivalent to $|\phi_0(0)\rangle$ because $\Omega_p(0) = 0$ at the initial time. The quantum adiabatic theorem states that if $\Omega_{p,S}$ are changed slowly enough and the initial state is an eigenstate $|\phi_0\rangle$, the state remains in the same eigenstate during the control. Therefore, when Ω_p increases sufficiently slowly, the population is gradually transferred from $|1, \downarrow\rangle$ to $|3, \downarrow\rangle$ [34,35]. We take $B_p^0 \gg B_S^0$ so that $|\phi_0\rangle \simeq |3, \downarrow\rangle$ at the final time. For $t > T_{\text{stepI}}$, $B_S^{(e)}$ and $B_p^{(e)}$ are to be gradually decreased to zero. The population of each state ($|i, \sigma\rangle$) is approximately unchanged if the duration of this process is long enough and $B_p^0 \gg B_S^0$ because the state remains in $|\phi_0(T_{\text{stepI}})\rangle$.

Figure 5 shows the time dependence of the envelope functions $B_p^{(e)}$ and $B_S^{(e)}$ (Figure 5a,b) and the corresponding time dependence of the population of each state (Figure 5c,d). We use $B_p^0 = 0.1$ mT and $B_S^0 = 0.0064$ mT so that the maximum value of $B_p^{(e)}$ is the same as the one used in π -pulse control and $B_p^0 \gg B_S^0$ at $t = T_{\text{stepI}}$. In the control with $T_{\text{stepI}} = 396$ μ s, the state deviates from $|\phi_0(t)\rangle$ due to unwanted nonadiabatic population transfer. Thus, the population of $|3, \downarrow\rangle$ at $t = T_{\text{stepI}}$ is less than 0.5. On the other hand, the dynamics are approximated by $|\phi_0(t)\rangle$, and the population of $|3, \downarrow\rangle$ is approximately 0.95 at $t = T_{\text{stepI}}$ for $T_{\text{stepI}} = 3960$ μ s. However, T_{stepI} required for the adiabatic dynamics is too long, in which case the efficiency will be degraded by relaxation and decoherence in actual experiments.

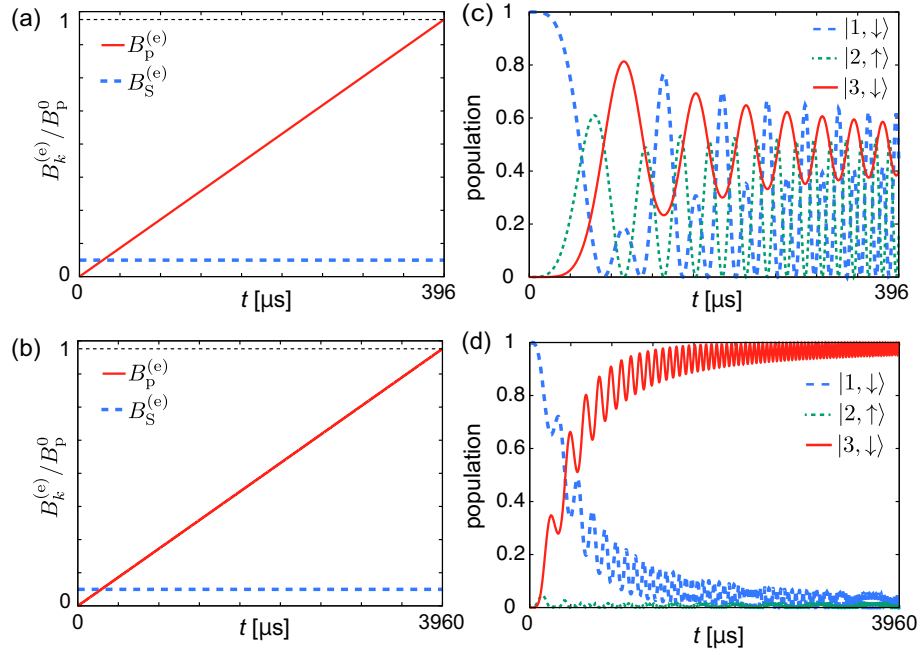


Figure 5. Envelope functions $B_k^{(e)}$ for $k = p, S$ normalized by B_p^0 for STIRAP with (a) $T_{\text{stepI}} = 396 \mu\text{s}$ and (b) $T_{\text{stepI}} = 3960 \mu\text{s}$. B_p^0 is the maximum amplitude of the pump field. The thin dotted line represents 1. Panels (c,d) are for the time dependencies of the populations corresponding to the envelope functions in the left panels.

3.2. Shortcuts to Adiabaticity

Shortcuts-to-adiabaticity (STA) protocols or assisted adiabatic transformations have been developed to reach the same target state as reference adiabatic dynamics starting from the given initial state, with overall weaker driving fields and/or shorter durations [65,66]. The STA protocols have been utilized for manipulations of, e.g., spin systems [67–71], electron spin of a single nitrogen-vacancy center in diamond [72,73], isolated atoms and molecules [74–78] and Bose-Einstein condensates [79–88]. Several STA protocols have been already demonstrated with STIRAP systems; for example, Loop STIRAP [89], counter-diabatic [74,75], fast-forward [90] and invariant-based engineering protocols [75,91].

We show the way to derive $\Omega_p(t)$ which approximately generates $|3, \downarrow\rangle$ in shorter time than that required for the adiabatic dynamics in Section 3.1 using the invariant based engineering protocol [75]. It is known that the state $|\varphi_0(t)\rangle$ of the form

$$|\varphi_0(t)\rangle = \begin{pmatrix} \cos \gamma(t) \cos \beta(t) \\ -i \sin \gamma(t) \\ -\cos \gamma(t) \sin \beta(t) \end{pmatrix}, \quad (14)$$

is a solution of the Schrödinger equation when

$$\begin{aligned} \Omega_S &= 2(\dot{\beta} \cot \gamma \cos \beta - \dot{\gamma} \sin \beta), \\ \Omega_P &= 2(\dot{\beta} \cot \gamma \sin \beta + \dot{\gamma} \cos \beta). \end{aligned} \quad (15)$$

These equations can be rewritten as

$$\begin{aligned} \dot{\gamma} &= \frac{1}{2}(\Omega_P \cos \beta - \Omega_S \sin \beta), \\ \dot{\beta} &= \frac{1}{2} \tan \gamma (\Omega_S \cos \beta + \Omega_P \sin \beta). \end{aligned} \quad (16)$$

We use γ defined by

$$\gamma = \gamma_0 \left[1 - \cos \left(\frac{2\pi t}{T_{\text{stepI}}} \right) \right] + \varepsilon, \quad (17)$$

where γ_0 and ε are constant parameters to be chosen so that

$$|\varphi_0(0)\rangle \simeq |1, \downarrow\rangle, \quad (18)$$

$$|\varphi_0(T_{\text{stepI}})\rangle \simeq -|3, \downarrow\rangle. \quad (19)$$

It is seen from Equation (14) that $|\varphi_0\rangle = |1, \downarrow\rangle$ if $\gamma = 0$ and $\beta = 0$, and that $|\varphi_0\rangle = -|3, \downarrow\rangle$ if $\gamma = 0$ and $\beta = \frac{\pi}{2}$. Thus, we set ε to be small, and set $\beta(0) = 0$. $\beta(t)$ is obtained by integrating Equation (16) using Equations (15) and (17). γ_0 is optimized so that $\beta(T_{\text{stepI}}) \simeq \frac{\pi}{2}$. Therefore, $B_p^{(e)}$ determined by Equations (3) and (15) can drive the initial state $|1, \downarrow\rangle$ approximately to the target state $|3, \downarrow\rangle$ up to an overall phase.

Typical time dependencies of $B_p^{(e)}$ and the population of each state are shown in Figure 6 for various T_{stepI} . The values of γ_0 and ε are chosen so that the maximum value of $B_p^{(e)}$ is the same as the one used in the π -pulse control. It is seen that population of $|2, \uparrow\rangle$ is small for $T_{\text{stepI}} = 396 \mu\text{s}$. On the other hand, the population of $|2, \uparrow\rangle$ is sizable around $t = T_{\text{stepI}}/2$ for $T_{\text{stepI}} = 198$ and $132 \mu\text{s}$ in contrast to the adiabatic dynamics analyzed in Section 3.1.

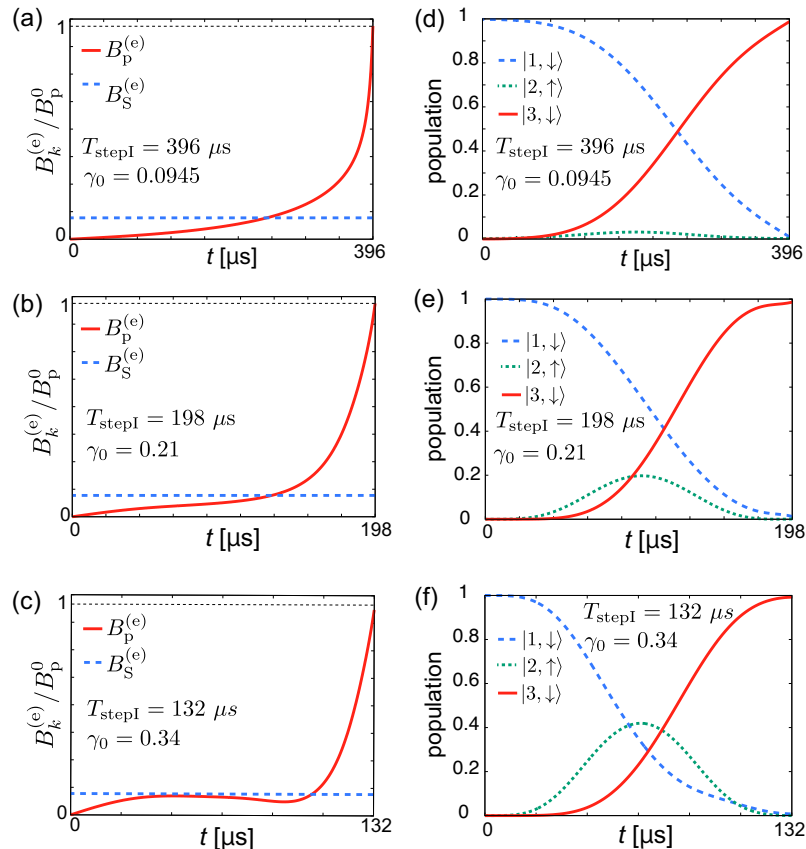


Figure 6. Envelope functions $B_k^{(e)}$ for $k = p, S$ normalized by B_p^0 for the invariant-based engineering protocol with (a) $T_{\text{stepI}} = 396 \mu\text{s}$, $\gamma_0 = 0.0945$ and $\varepsilon = 0.02$; (b) $T_{\text{stepI}} = 198 \mu\text{s}$, $\gamma_0 = 0.21$ and $\varepsilon = 0.02$; and (c) $T_{\text{stepI}} = 132 \mu\text{s}$, $\gamma_0 = 0.34$ and $\varepsilon = 0.02$. B_p^0 is the maximum amplitude of the pump field. The thin dotted line represents 1. (d)–(f) Time dependencies of the populations corresponding to the envelope functions in the left panels.

For $t > T_{\text{stepI}}$, $B_S^{(e)}$ and $B_P^{(e)}$ are to be gradually decreased to zero. The population of each state is approximately unchanged under this. This process is insensitive to the details of B_S^0 and B_P^0 as long as $B_S^0 \ll B_P^0$, and the duration of the process is much shorter than T_{stepI} . Therefore, the duration of this process is negligible (see Appendix A).

4. Robustness of Control

Robustness of the control against the pulse amplitude error, the effect of the relaxation of excited states and the effect of the dephasing of spin to the control efficiency are examined in this section.

4.1. The Effect of the Error of the Pulse Amplitude

We multiply the pump field by λ to analyze the robustness of the control against the pulse amplitude error. The fidelities of the π -pulse control and the invariant-based engineering protocol are defined by the population of $|2, \uparrow\rangle$ and the population of $|3, \downarrow\rangle$ at $t = T_{\text{stepI}}$, respectively. Figure 7 shows the fidelity as a function of λ for the π -pulse control and the invariant-based engineering protocol. It is seen that the fidelity of the latter is higher than the one of the former in a wide range of λ values, while the maximum value of the fidelity for the former is higher than the one of the latter. This shows that the invariant-based engineering protocol is robust against the pulse amplitude error compared to the π -pulse control.

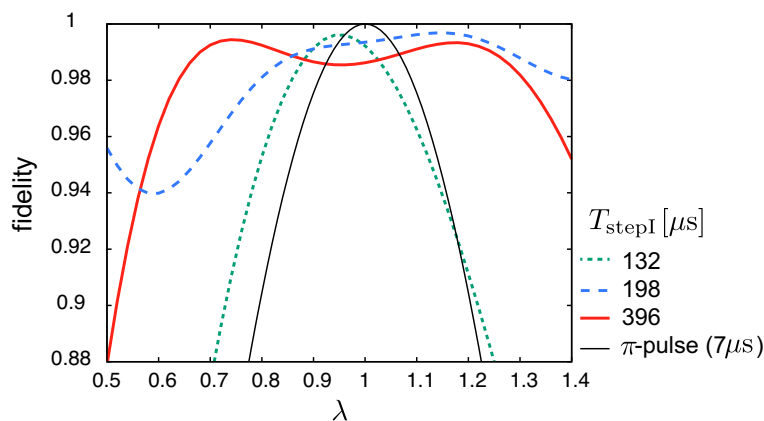


Figure 7. Dependence of the fidelity at $t = T_{\text{stepI}}$ on λ for the π -pulse and the invariant-based engineering protocols. λ is the multiplicative factor of amplitude error, where $\lambda = 1$ corresponds to no error.

4.2. The Effect of the Relaxation of Excited States

We examine the effect of the relaxation of excited states using the master equation [92]:

$$\frac{d\rho}{dt} = -i[H, \rho] + \mathcal{L}[\rho], \tag{20}$$

where ρ is the density operator. $\mathcal{L}[\rho]$ is given by

$$\begin{aligned} \mathcal{L}[\rho] = & \frac{\kappa}{2} \left([a_{\downarrow} \rho, a_{\downarrow}^{\dagger}] + [a_{\downarrow}, \rho a_{\downarrow}^{\dagger}] \right) \\ & + \frac{\kappa}{2} \left([a_{\uparrow} \rho, a_{\uparrow}^{\dagger}] + [a_{\uparrow}, \rho a_{\uparrow}^{\dagger}] \right) \end{aligned} \tag{21}$$

with the relaxation rate κ , where $a_{\downarrow(\uparrow)}$ is the annihilation operator represented as

$$a_{\downarrow(\uparrow)} = |1, \downarrow(\uparrow)\rangle \langle 2, \downarrow(\uparrow)| + \sqrt{2} |2, \downarrow(\uparrow)\rangle \langle 3, \downarrow(\uparrow)|. \tag{22}$$

$a_{\downarrow(\uparrow)}$ corresponds to spin-down (up) state. We neglect the effect of spin relaxation assuming that the relaxation rate of excited states is much faster than the spin relaxation rate. The effect of the spin dephasing effect is studied in the next subsection.

Figure 8 shows the fidelity of the π -pulse control and the invariant-based engineering protocol as a function of κ . It is seen that the π -pulse control is much more robust against the relaxation than the invariant-based engineering protocol because its control duration T_{stepI} is much shorter than the one for the invariant-based engineering protocol.

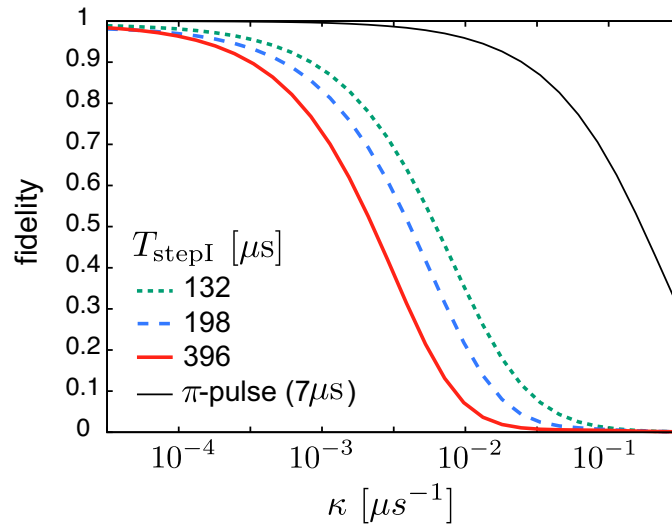


Figure 8. Dependence of the fidelity at $t = T_{\text{stepI}}$ on κ for the π -pulse and the invariant-based engineering protocols.

4.3. Effect of Dephasing of Spin

We examine the effect of the dephasing of spin using the master Equation [92]:

$$\frac{d\rho}{dt} = -i[H, \rho] + \mathcal{L}_p[\rho], \tag{23}$$

where $\mathcal{L}_p[\rho]$ is given by

$$\mathcal{L}_p[\rho] = -\frac{\gamma_p}{4} [\sigma_z, [\sigma_z, \rho]] \tag{24}$$

with the dephasing rate γ_p . We neglect the effect of the other relaxations.

We assume that the initial state is a superposition of spin up and down states represented as

$$|\Psi_{\text{ini}}\rangle = \frac{1}{\sqrt{2}}|1 \downarrow\rangle + \frac{1}{\sqrt{2}}|1 \uparrow\rangle. \tag{25}$$

The target states for the π -pulse control and the invariant-based engineering protocol are represented as

$$|\Psi_{\text{tar}}\rangle = -\frac{i}{\sqrt{2}}|2, \uparrow\rangle + \frac{1}{\sqrt{2}}|1, \uparrow\rangle \tag{26}$$

and

$$|\Psi_{\text{tar}}\rangle = -\frac{1}{\sqrt{2}}|3 \downarrow\rangle + \frac{1}{\sqrt{2}}|1 \uparrow\rangle, \tag{27}$$

respectively. Note that the state $|1, \downarrow\rangle$ is transferred to $|2, \uparrow\rangle$ in the π -pulse case without decoherence. On the other hand, the state $|1, \downarrow\rangle$ is transferred to $|3, \downarrow\rangle$ in the invariant-based engineering protocol if there is no decoherence. The phases of $|2, \uparrow\rangle$ in Equation (26) and $|3, \downarrow\rangle$ in Equation (27) appear after the controls without decoherence. We define the fidelity, F , of the controls as

$$F = \langle \Psi_{\text{tar}} | \rho(T_{\text{stepI}}) | \Psi_{\text{tar}} \rangle, \quad (28)$$

and define the coherence, C , at $t = T_{\text{stepI}}$ for the π -pulse control as

$$C = |\langle 2, \uparrow | \rho(T_{\text{stepI}}) | 1, \downarrow \rangle|. \quad (29)$$

We define the coherence for the invariant-based engineering protocol as

$$C = |\langle 3, \downarrow | \rho(T_{\text{stepI}}) | 1, \downarrow \rangle|. \quad (30)$$

Figure 9a shows the dependence of the fidelity of the the π -pulse and the invariant-based engineering protocols on γ_p . It is seen that the fidelity decreases with the increase of γ_p . Crossings of the fidelity of the invariant-based engineering protocols are observed when γ_p increases. Although we could not have a clear reason for this, we found that the main contribution to the fidelity came from the diagonal elements of the density matrix, and the off-diagonal elements were approximately vanishing in that parameter region. Figure 9b shows the dependence of the coherence of the the π -pulse and the invariant-based engineering protocols on γ_p . The coherence decreases as γ_p increases. The fidelity and coherence of the π -pulse control is higher than the invariant-based engineering protocol because of the short control time. Increasing the amplitude of the oscillating magnetic field can shorten the control time, leading to improvement of the control fidelity.

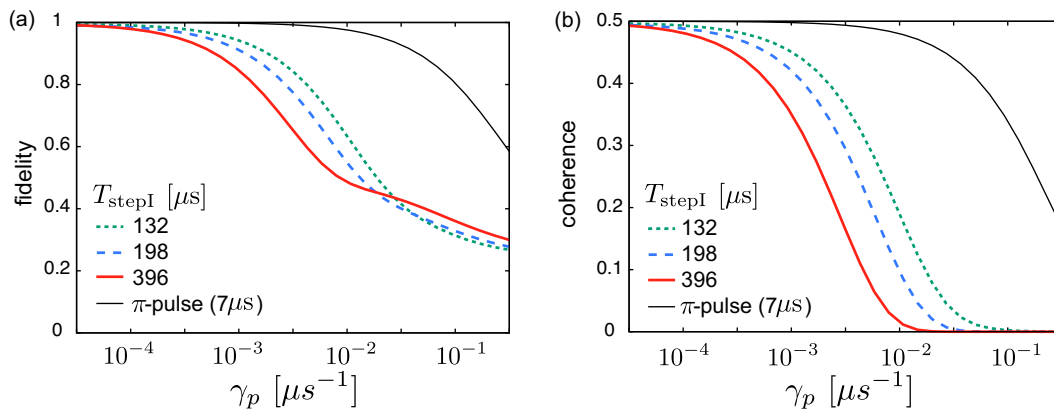


Figure 9. Dependence of the fidelity (a) and the coherence (b) at $t = T_{\text{stepI}}$ on γ_p for the π -pulse and the invariant-based engineering protocols.

5. Conclusions

In the research presented, we studied spin-selective coherent electron transfer in a quantum dot array with time-dependent tuning of the driving field. The electron is excited and transferred into different quantum dots (Dots 1 and 2 in Figure 1c) depending on the initial electron spin. We have proposed two different methods: the π -pulse control and the invariant-based engineering protocol. The π -pulse control offers fast transport, while a robust control against the error of the pulse area of the control field is achieved by the invariant-based engineering protocol, although the manipulation time is longer than that of the π -pulse control. We also studied the effect of the relaxation of excited states and the dephasing of spin to the control efficiency. The π -pulse control offers robustness against the relaxation of excited states due to its short control time, while the invariant-based engineering protocol is sensitive to the relaxation and the dephasing rates.

In Section 3 we studied the effective three-level-system where the constant coupling between states $|2, \uparrow\rangle$ and $|3, \downarrow\rangle$ is caused by an external field. We emphasize that the control developed with constant Ω_S can also be applied to systems where two degenerate energy levels have an intrinsic fixed coupling. Such a condition can be realized, e.g., in a cavity QED system where an atom is coupled to a resonant cavity mode [93], and in a circuit QED system where an artificial atom is coupled to a tunable resonator mode [94,95].

In our scheme, a combined quantum dot (Dot 0) is used. It is known that making the dot size large is difficult in silicon, where the electron wave function needs to be tightly confined. In that sense the π -pulse control is better than the invariant-based engineering protocol, because the former one utilizes only up to the first excited state which is less spread-out than the second excited state. The smaller dot size requires the larger frequency of the AC magnetic field in our scheme. Thus, the size of the dot is limited by the experimental feasibility of the frequency of the AC magnetic field. On the other hand, the GaAs system can form a large dot, although the short coherence time is problematic [96]. The spin-orbit coupling [97,98] could be problematic in Step II. However, we believe that the study of clever pulse schemes to mitigate spin-orbit coupling is beyond the scope of the paper. This will indeed be something of interest for further investigation.

Author Contributions: S.M. developed and analyzed the model. K.Y.T. and M.N. contributed to the development of the model and data analysis. All authors commented on and edited the manuscript of which the original draft was written by S.M. All authors have read and agreed to the published version of the manuscript.

Funding: S.M. acknowledges the support from JST ERATO (grant number JPMJER1601) and JSPS KAKENHI (grant number 18K03486). K.Y.T. acknowledges the support from the Academy of Finland (grant numbers 308161, 314302 and 316551).

Conflicts of Interest: The authors declare no conflict of interest.

Abbreviations

The following abbreviations are used in this manuscript:

STIRAP	stimulated Raman adiabatic passage
STA	shortcuts to adiabaticity
RWA	rotating wave approximation

Appendix A. End of Step I

For $t > T_{\text{stepI}}$, $B_S^{(e)}$ and $B_P^{(e)}$ are gradually decreased to zero. To simulate this process, we assume

$$\begin{aligned}
 B_S^{(e)}(t) &= B_S^0 e^{-(t-T_{\text{stepI}})/\tau} && \text{for } t > T_{\text{stepI}}, \\
 B_P^{(e)}(t) &= \begin{cases} B_P^0 & \text{for } T_{\text{stepI}} < t \leq T_{\text{stepI}} + \tau, \\ B_P^0 e^{-(t-T_{\text{stepI}}-\tau)/\tau} & \text{for } t > T_{\text{stepI}} + \tau, \end{cases}
 \end{aligned}
 \tag{A1}$$

where τ characterizes the decay time of the envelope functions. $B_S^{(e)}$ and $B_P^{(e)}$ start to decrease at $t = T_{\text{stepI}}$ and $T_{\text{stepI}} + \tau$, respectively.

Figure A1a–c show the envelope functions $B_P^{(e)}$ and $B_S^{(e)}$ for the invariant-based engineering protocol with $T_{\text{stepI}} = 198 \mu\text{s}$ and $T_{\text{stepII}} = 131 \mu\text{s}$. The time dependence of the envelope functions for $t \leq T_{\text{stepI}}$ are the same as the ones in Figure 6b,c. Figure A1d–f show that the populations are almost unchanged for $t > T_{\text{stepI}}$, while $B_P^{(e)}$ and $B_S^{(e)}$ are decreased. This process is insensitive to τ , and the duration of the process can be much shorter than T_{stepI} .

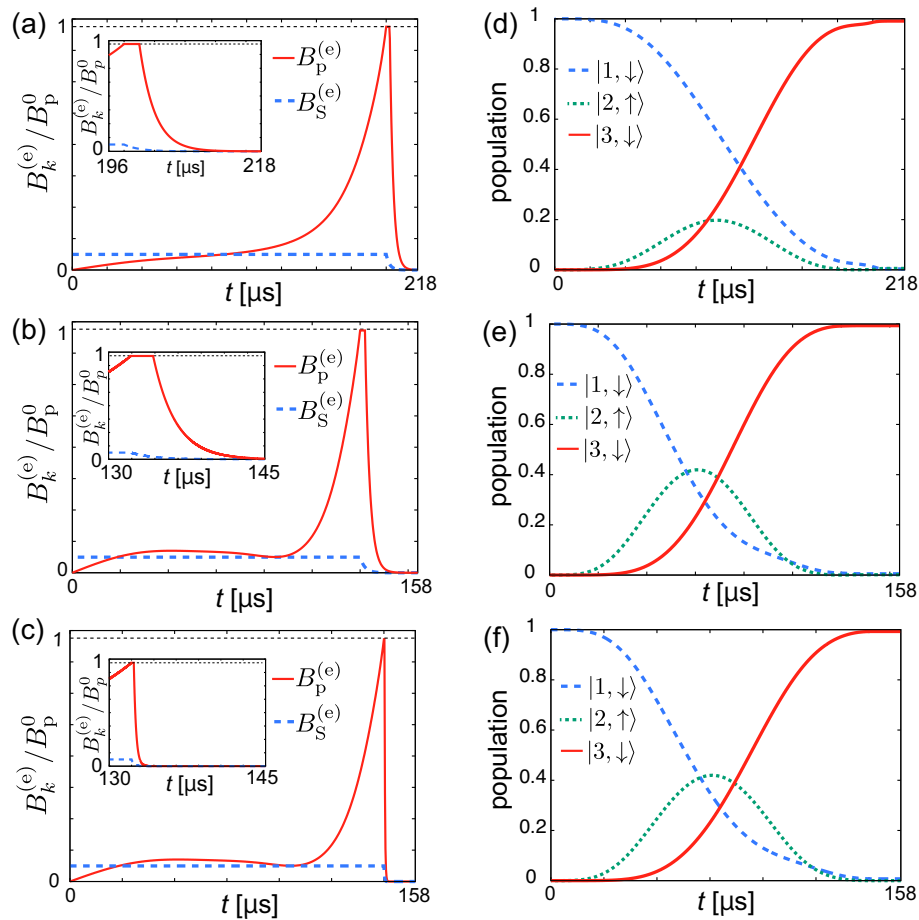


Figure A1. Envelope functions $B_k^{(e)}$ for $k = p, S$ normalized by B_p^0 for the invariant-based engineering protocol with (a) $T_{\text{stepI}} = 198 \mu\text{s}$, $\gamma_0 = 0.21$, $\varepsilon = 0.02$ and $\tau = 2 \mu\text{s}$; (b) $T_{\text{stepI}} = 132 \mu\text{s}$, $\gamma_0 = 0.34$, $\varepsilon = 0.02$ and $\tau = 2 \mu\text{s}$; (c) $T_{\text{stepII}} = 132 \mu\text{s}$, $\gamma_0 = 0.34$, $\varepsilon = 0.02$ and $\tau = 0.2 \mu\text{s}$. B_p^0 is the maximum amplitude of the pump field. The thin dotted line represents 1. (d)–(f) Time dependence of the eigenstate populations corresponding to the envelopes in the left panels.

References

1. Loss, D.; DiVincenzo, D.P. Quantum computation with quantum dots. *Phys. Rev. A* **1998**, *57*, 120–126. [[CrossRef](#)]
2. Fowler, A.G.; Mariantoni, M.; Martinis, J.M.; Cleland, A.N. Surface codes: Towards practical large-scale quantum computation. *Phys. Rev. A* **2012**, *86*, 032324–032371. [[CrossRef](#)]
3. Morello, A.; Pla, J.J.; Zwanenburg, F.A.; Chan, K.W.; Tan, K.Y.; Huebl, H.; Möttönen, M.; Nugroho, C.D.; Yang, C.; van Donkelaar, J.A.; et al. Single-shot readout of an electron spin in silicon. *Nature* **2010**, *467*, 687–691. [[CrossRef](#)] [[PubMed](#)]
4. Pla, J.J.; Tan, K.Y.; Dehollain, J.P.; Lim, W.H.; Morton, J.J.L.; Jamieson, D.N.; Dzurak, A.S.; Morello, A. A single-atom electron spin qubit in silicon. *Nature* **2012**, *489*, 541–545. [[CrossRef](#)] [[PubMed](#)]
5. Muhonen, J.T.; Dehollain, J.P.; Laucht, A.; Hudson, F.E.; Kalra, R.; Sekiguchi, T.; Itoh, K.M.; Jamieson, D.N.; McCallum, J.C.; Dzurak, A.S.; et al. Storing quantum information for 30 seconds in a nanoelectronic device. *Nat. Nanotech.* **2014**, *9*, 986–991. [[CrossRef](#)] [[PubMed](#)]
6. Maune, B.M.; Borselli, M.G.; Huang, B.; Ladd, T.D.; Deelman, P.W.; Holabird, K.S.; Kiselev, A.A.; Alvarado-Rodriguez, I.; Ross, R.S.; Schmitz, A.E.; et al. Coherent singlet-triplet oscillations in a silicon-based double quantum dot. *Nature* **2012**, *481*, 344–347. [[CrossRef](#)]
7. Veldhorst, M.; Hwang, J.C.C.; Yang, C.H.; Leenstra, A.W.; de Ronde, B.; Dehollain, J.P.; Muhonen, J.T.; Hudson, F.E.; Itoh, K.M.; Morello, A.; et al. An addressable quantum dot qubit with fault-tolerant control-fidelity. *Nat. Nanotechnol.* **2014**, *9*, 981–985. [[CrossRef](#)]

8. Kawakami, E.; Scarlino, P.; Ward, D.R.; Braakman, F.R.; Savage, D.E.; Lagally, M.G.; Friesen, M.; Coppersmith, S.N.; Eriksson M.A.; Vandersypen, L.M.K. Electrical control of a long-lived spin qubit in a Si/SiGe quantum dot. *Nat. Nanotechnol.* **2014**, *9*, 666–670. [[CrossRef](#)]
9. Itoh, K.M.; Watanabe, H. Isotope engineering of silicon and diamond for quantum computing and sensing applications. *MRS Commun.* **2014**, *4*, 143–157. [[CrossRef](#)]
10. Urdampilleta, M.; Niegemann, D.J.; Chanrion, E.; Jadot, B.; Spence, C.; Mortemousque, P.; Bäuerle, C.; Hutin, L.; Bertrand, B.; Barraud, S.; et al. Gate-based high fidelity spin readout in a CMOS device. *Nat. Nanotechnol.* **2019**, *14*, 737–741. [[CrossRef](#)]
11. Yang, C.H.; Leon, R.C.C.; Hwang, J.C.C.; Saraiva, A.; Tanttu, T.; Huang, W.; Lemyre, J.C.; Chan, K.W.; Tan, K.Y.; Hudson, F.E.; et al. Silicon quantum processor unit cell operation above one Kelvin. *arXiv* **2019**, arXiv:1902.09126.
12. Masuda, S.; Tan, K.Y.; Nakahara, M. Spin-selective electron transfer in a quantum dot array. *Phys. Rev. B* **2018**, *97*, 045418–045431. [[CrossRef](#)]
13. Noiri, A.; Yoneda, J.; Nakajima, T.; Otsuka, T.; Delbecq, M.R.; Takeda, K.; Amaha, S.; Allison, G.; Ludwig, A.; Wieck, A.D.; et al. Coherent electron-spin-resonance manipulation of three individual spins in a triple quantum dot. *Appl. Phys. Lett.* **2016**, *108*, 153101–153105. [[CrossRef](#)]
14. Takeda, K.; Kamioka, J.; Otsuka, T.; Yoneda, J.; Nakajima, T.; Delbecq, M.R.; Amaha, S.; Allison, G.; Kodera, T.; Oda, S.; et al. A fault-tolerant addressable spin qubit in a natural silicon quantum dot. *Sci. Adv.* **2016**, *2*, e1600694–e1600699. [[CrossRef](#)] [[PubMed](#)]
15. Harvey-Collard, P.; Tobias Jacobson, N.; Rudolph, M.; Dominguez, J.; Ten Eyck, G.A.; Wendt, J.R.; Pluym, T.; King Gamble, J.; Lilly, M.P.; Pioro-Ladrière, M.; et al. Coherent coupling between a quantum dot and a donor in silicon. *Nat. Commun.* **2017**, *8*, 1029–1034. [[CrossRef](#)]
16. Veldhorst, M.; Yang, C.H.; Hwang, J.C.C.; Huang, W.; Dehollain, J.P.; Muhonen, J.T.; Simmons, S.; Laucht, A.; Hudson, F.E.; Itoh, K.M.; et al. A two-qubit logic gate in silicon. *Nature* **2015**, *526*, 410–414. [[CrossRef](#)]
17. Kouwenhoven, L.P.; Johnson, A.T.; van der Vaart, N.C.; Harmans, C.J.P.M.; Foxon, C.T. Quantized current in a quantum-dot turnstile using oscillating tunnel barriers. *Phys. Rev. Lett.* **1991**, *67*, 1626–1629. [[CrossRef](#)]
18. Blumenthal, M.D.; Kaestner, B.; Li, L.; Giblin, S.; Janssen, T.J.B.M.; Pepper, M.; Anderson, D.; Jones G.; Ritchie, D.A. Gigahertz quantized charge pumping. *Nat. Phys.* **2007**, *3*, 343–347. [[CrossRef](#)]
19. Jehl, X.; Voisin, B.; Charron, T.; Clapera, P.; Ray, S.; Roche, B.; Sanquer, M.; Djordjevic, S.; Devoille, L.; Wacquez, R.; et al. Hybrid Metal-Semiconductor Electron Pump for Quantum Metrology. *Phys. Rev. X* **2013**, *3*, 021012–021023. [[CrossRef](#)]
20. Connolly, M.R.; Chiu, K.L.; Giblin, S.P.; Kataoka, M.; Fletcher, J.D. Chua, C.; Griffiths, J.P.; Jones, G.A.C.; Fal’ko, V.I.; Smith C.G.; et al. Gigahertz quantized charge pumping in graphene quantum dots. *Nat. Nanotechnol.* **2013**, *8*, 417–420. [[CrossRef](#)]
21. Rossi, A.; Tanttu, T.; Tan, K.Y.; Iisakka, I.; Zhao, R.; Chan, K.W.; Tettamanzi, G.C.; Rogge, S.; Dzurak, A.S.; Möttönen, M. An Accurate Single-Electron Pump Based on a Highly Tunable Silicon Quantum Dot. *Nano Lett.* **2014**, *14*, 3405–3411. [[CrossRef](#)] [[PubMed](#)]
22. Pekola, J.; Saira, O.-P.; Maisi, V.F.; Kempainen, A.; Möttönen, M.; Pashkin, Y.A.; Averin, D.V. Single-electron current sources: Toward a refined definition of the ampere. *Rev. Mod. Phys.* **2013**, *86*, 1421–1472. [[CrossRef](#)]
23. Tanttu, T.; Rossi, A.; Tan, K.Y.; Huhtinen, K.-E.; Chan, K.W.; Möttönen, M.; Dzurak, A.S. Electron counting in a silicon single-electron pump. *New J. Phys.* **2015**, *17*, 103030–103035. [[CrossRef](#)]
24. Chan, K.W.; Möttönen, M.; Kempainen, A.; Lai, N.S.; Tan, K.Y.; Lim W.H.; Dzurak, A.S. Single-electron shuttle based on a silicon quantum dot. *Appl. Phys. Lett.* **2011**, *98*, 212103–212105. [[CrossRef](#)]
25. Baart, T.A.; Shafiei, M.; Fujita, T.; Reichl, C.; Wegscheider, W.; Vandersypen, L.M.K. Single-spin CCD. *Nat. Nanotechnol.* **2016**, *11*, 330–334. [[CrossRef](#)] [[PubMed](#)]
26. Flentje, H.; Mortemousque, P.-A.; Thalineau, R.; Ludwig, A.; Wieck, A.D.; Bäuerle, C.; Meunier, T. Coherent long-distance displacement of individual electron spins. *Nat. Commun.* **2017**, *8*, 501. [[CrossRef](#)] [[PubMed](#)]
27. Jaksch, D.; Briegel, H.-J.; Cirac, J.I.; Gardiner, C.W.; Zoller, P. Entanglement of Atoms via Cold Controlled Collisions. *Phys. Rev. Lett.* **1999**, *82*, 1975–1978. [[CrossRef](#)]
28. Lapasar, E.H.; Kasamatsu, K.; Kondo, Y.; Nakahara, M.; Ohmi, T. Scalable Neutral Atom Quantum Computer with Interaction on Demand: Proposal for Selective Application of Two-Qubit Gate. *J. Phys. Soc. Jpn.* **2011**, *80*, 114003–114012. [[CrossRef](#)]

29. Lapasar, E.H.; Kasamatsu, K.; Nic Chormaic, S.; Takui, T.; Kondo, Y.; Nakahara, M.; Ohmi, T. Two-Qubit Gate Operation on Selected Nearest-Neighbor Neutral Atom Qubits *J. Phys. Soc. Jpn.* **2014**, *83*, 044005–044010. [[CrossRef](#)]
30. Sarovar, M.; Young, K.C.; Schenkel, T.; Whaley, K.B. Quantum nondemolition measurements of single donor spins in semiconductors. *Phys. Rev. B* **2008**, *78*, 245302–245309. [[CrossRef](#)]
31. Puri, S.; McMahon, P.L.; Yamamoto, Y. Single-shot quantum nondemolition measurement of a quantum-dot electron spin using cavity exciton-polaritons. *Phys. Rev. B* **2014**, *90*, 155421–155425. [[CrossRef](#)]
32. Nakajima, T.; Noiri, A.; Yoneda, J.; Delbecq, M.R.; Stano, P.; Otsuka, T.; Takeda, K.; Amaha, S.; Allison, G.; Kawasaki, K.; et al. Quantum non-demolition measurement of an electron spin qubit. *Nat. Nanotechnol.* **2019**, *14*, 555–560. [[CrossRef](#)] [[PubMed](#)]
33. Gaubatz, U.; Rudecki, P.; Schiemann, S.; Bergmann, K. Population transfer between molecular vibrational levels by stimulated Raman scattering with partially overlapping laser fields. A new concept and experimental results. *J. Chem. Phys.* **1990**, *92*, 5363–5376. [[CrossRef](#)]
34. Bergmann, K.; Theuer, H.; Shore, B.W. Coherent population transfer among quantum states of atoms and molecules. *Rev. Mod. Phys.* **1998**, *70*, 1003–1025. [[CrossRef](#)]
35. Vitanov, N.V.; Halfmann, T.; Shore, B.W.; Bergmann, K. Laser-Induced Population Transfer by Adiabatic Passage Techniques. *Ann. Rev. Phys. Chem.* **2001**, *52*, 763–809. [[CrossRef](#)]
36. Greentree, A.D.; Cole, J.H.; Hamilton, A.R.; Hollenberg, L.C.L. Coherent electronic transfer in quantum dot systems using adiabatic passage. *Phys. Rev. B* **2004**, *70*, 235317–235322. [[CrossRef](#)]
37. Jong, L.M.; Greentree, A.D.; Conrad, V.I.; Hollenberg, L.C.L.; Jamieson, D.N. Coherent tunneling adiabatic passage with the alternating coupling scheme. *Nanotechnology* **2009**, *20*, 405402–405409. [[CrossRef](#)]
38. Eckert, K.; Lewenstein, M.; Corbalán, R.; Birkl, G.; Ertmer, W.; Mompert, J. Three-level atom optics via the tunneling interaction. *Phys. Rev. A* **2004**, *70*, 023606–023610. [[CrossRef](#)]
39. Eckert, K.; Mompert, J.; Corbalán, R.; Lewenstein, M.; Birkl, G. Three level atom optics in dipole traps and waveguides. *Opt. Commun.* **2006**, *264*, 264–270. [[CrossRef](#)]
40. Opatrný, T.; Das, K.K. Conditions for vanishing central-well population in triple-well adiabatic transport. *Phys. Rev. A* **2009**, *79*, 012113–012119. [[CrossRef](#)]
41. O’Sullivan, B.; Morrissey, P.; Morgan, T.; Busch, T. Using adiabatic coupling techniques in atom-chip waveguide structures. *Phys. Scr.* **2010**, *140*, 014029–014034. [[CrossRef](#)]
42. Morgan, T.; O’Sullivan, B.; Busch, T. Coherent adiabatic transport of atoms in radio-frequency traps. *Phys. Rev. A* **2011**, *83*, 053620–053625. [[CrossRef](#)]
43. Morgan, T.; O’Riordan, L.J.; Crowley, N.; O’Sullivan, B.; Busch, T. Coherent transport by adiabatic passage on atom chips. *Phys. Rev. A* **2013**, *88*, 053618–053623. [[CrossRef](#)]
44. Graefe, E.M.; Korsch, H.J.; Witthaut, D. Mean-field dynamics of a Bose-Einstein condensate in a time-dependent triple-well trap: Nonlinear eigenstates, Landau-Zener models, and stimulated Raman adiabatic passage. *Phys. Rev. A* **2006**, *73*, 013617–013622. [[CrossRef](#)]
45. Rab, M.; Cole, J.H.; Parker, N.G.; Greentree, A.D.; Hollenberg, L.C.L.; Martin, A.M. Spatial coherent transport of interacting dilute Bose gases. *Phys. Rev. A* **2008**, *77*, 061602–061605. [[CrossRef](#)]
46. Nesterenko, V.O.; Novikov, A.N.; de Souza Cruz, F.F.; Lapolli, E.L. Tunneling and transport dynamics of trapped Bose-Einstein condensates. *Laser Phys.* **2009**, *19*, 616–624. [[CrossRef](#)]
47. Rab, M.; Hayward, A.L.C.; Cole, J.H.; Greentree, A.D.; Martin, A.M. Interferometry using adiabatic passage in dilute-gas Bose-Einstein condensates. *Phys. Rev. A* **2012**, *86*, 063605–063614. [[CrossRef](#)]
48. Coulston, G.W.; Bergmann, K. Population transfer by stimulated Raman scattering with delayed pulses: Analytical results for multilevel systems. *J. Chem. Phys.* **1994**, *96*, 3467–3475. [[CrossRef](#)]
49. Martin, J.; Shore, B.W.; Bergmann, K. Coherent population transfer in multilevel systems with magnetic sublevels. III. Experimental results. *Phys. Rev. A* **1996**, *54*, 1556–1569. [[CrossRef](#)]
50. Halfmann, T.; Bergmann, K. Coherent population transfer and dark resonances in SO₂. *J. Chem. Phys.* **1996**, *104*, 7068–7072. [[CrossRef](#)]
51. Malinovsky, V.S.; Tannor, D.J. Simple and robust extension of the stimulated Raman adiabatic passage technique to *N*-level systems. *Phys. Rev. A* **1997**, *56*, 4929–4937. [[CrossRef](#)]
52. Kobrak, M.N.; Rice, S.A. Selective photochemistry via adiabatic passage: An extension of stimulated Raman adiabatic passage for degenerate final states *Phys. Rev. A* **1998**, *57*, 2885–2894. [[CrossRef](#)]

53. Kurkal V.; Rice, S.A. Sequential STIRAP-based control of the HCN→CNH isomerization. *Chem. Phys. Lett.* **2001**, *344*, 125–137. [[CrossRef](#)]
54. Cheng, T.; Darmawan, H.; Brown, A. Stimulated Raman adiabatic passage in molecules: The effects of background states. *Phys. Rev. A* **2007**, *75*, 013411–013421. [[CrossRef](#)]
55. Jakubetz, W. Limitations of STIRAP-like population transfer in extended systems: The three-level system embedded in a web of background states. *J. Chem. Phys.* **2012**, *137*, 224312–224327. [[CrossRef](#)]
56. Kumar, K.S.; Vepsäläinen, A.; Danilin, S.; Paraoanu, G.S. Stimulated Raman adiabatic passage in a three-level superconducting circuit. *Nat. Commun.* **2016**, *7*, 10628. [[CrossRef](#)]
57. Dittmann, P.; Pesl, F.P.; Martin, J.; Coulston, G.W.; He, G.Z.; Bergmann, K. The effect of vibrational excitation ($3 \leq v' \leq 19$) on the reaction $\text{Na}_2(v') + \text{Cl} \rightarrow \text{NaCl} + \text{Na}^*$. *J. Chem. Phys.* **1992**, *97*, 9472–9475. [[CrossRef](#)]
58. Kulin, S.; Saubamea, B.; Peik, E.; Lawall, J.; Hijmans, T.W.; Leduc, M.; Cohen-Tannoudji, C. Coherent Manipulation of Atomic Wave Packets by Adiabatic Transfer. *Phys. Rev. Lett.* **1997**, *78*, 4185–4188. [[CrossRef](#)]
59. Longhi, S.; Della Valle, G.; Ornigotti, M.; Laporta, P. Coherent tunneling by adiabatic passage in an optical waveguide system. *Phys. Rev. B* **2007**, *76*, 201101–201104. [[CrossRef](#)]
60. Lahini, Y.; Pozzi, F.; Sorel, M.; Morandotti, R.; Christodoulides, D.N.; Silberberg, Y. Effect of Nonlinearity on Adiabatic Evolution of Light. *Phys. Rev. Lett.* **2008**, *101*, 193901–193904. [[CrossRef](#)]
61. Menchon-Enrich, R.; Llobera, A.; Cadarso, V.J.; Mompert, J.; Ahufinger, V. Adiabatic Passage of Light in CMOS-Compatible Silicon Oxide Integrated Rib Waveguides. *IEEE Photonics Technol. Lett.* **2012**, *24*, 536–538. [[CrossRef](#)]
62. Menchon-Enrich, R.; Llobera, A.; Vila-Planas, J.; Cadarso, V.J.; Mompert, J.; Ahufinger, V. Light spectral filtering based on spatial adiabatic passage. *Light Sci. Appl.* **2013**, *2*, e90–e97. [[CrossRef](#)]
63. Menchon-Enrich, R.; Mompert, J.; Ahufinger, V. Spatial adiabatic passage processes in sonic crystals with linear defects. *Phys. Rev. B* **2014**, *89*, 094304–094313. [[CrossRef](#)]
64. Hollenberg, L.C.L.; Greentree, A.D.; Fowler, A.G.; Wellard, C.J. Two-dimensional architectures for donor-based quantum computing. *Phys. Rev. B* **2006**, *74*, 045311–045318. [[CrossRef](#)]
65. Torrontegui, E.; Ibáñez, S.; Martínez-Garaot, S.; Modugno, M.; del Campo, A.; Guéry-Odelin, D.; Ruschhaupt, A.; Chen, X.; Muga, J.G. Shortcuts to Adiabaticity. *Adv. Atom. Mol. Opt. Phys.* **2013**, *62*, 117–169.
66. Masuda, S.; Rice, S.A. Controlling Quantum Dynamics with Assisted Adiabatic Processes. *Adv. Chem. Phys.* **2016**, *159*, 51–135.
67. Berry, M. Transitionless quantum driving. *J. Phys. A Math.Gen.* **2009**, *42*, 365303–365311. [[CrossRef](#)]
68. del Campo, A.; Rams, M.M.; Zurek, W.H. Assisted Finite-Rate Adiabatic Passage Across a Quantum Critical Point: Exact Solution for the Quantum Ising Model. *Phys. Rev. Lett.* **2012**, *109*, 115703–115707. [[CrossRef](#)]
69. Fasihi, M.-A.; Wan Y.; Nakahara, M. Non-adiabatic Fast Control of Mixed States Based on Lewis-Riesenfeld Invariant. *J. Phys. Soc. Jpn.* **2012**, *81*, 024007–024014. [[CrossRef](#)]
70. Takahashi, K. Transitionless quantum driving for spin systems. *Phys. Rev. E* **2013**, *87*, 062117–062125. [[CrossRef](#)]
71. Setiawan, I.; Gunara, B.E.; Masuda, S.; Nakamura, K. Fast forward of the adiabatic spin dynamics of entangled states. *Phys. Rev. A* **2017**, *96*, 052106–052116. [[CrossRef](#)]
72. Zhang, J.; Shim, J.H.; Niemeyer, I.; Taniguchi, T.; Teraji, T.; Abe, H.; Onoda, S.; Yamamoto, T.; Ohshima, T.; Isoya, J.; et al. Experimental Implementation of Assisted Quantum Adiabatic Passage in a Single Spin. *Phys. Rev. Lett.* **2013**, *110*, 240501–240505. [[CrossRef](#)] [[PubMed](#)]
73. Zhou, B.B.; Baksic, A.; Ribeiro, H.; Yale, C.G.; Joseph Heremans, F.; Jerger, P.C.; Auer, A.; Burkard, G.; Clerk, A.A.; Awschalom, D.D. Accelerated quantum control using superadiabatic dynamics in a solid-state lambda system. *Nat. Phys.* **2016**, *13*, 330–334. [[CrossRef](#)]
74. Demirplak, M.; Rice, S.A. Adiabatic Population Transfer with Control Fields. *J. Phys. Chem. A* **2003**, *107*, 9937–9945. [[CrossRef](#)]
75. Chen, X.; Lizuain, I.; Ruschhaupt, A.; Guéry-Odelin, D.; Muga, J.G. Shortcut to Adiabatic Passage in Two- and Three-Level Atoms. *Phys. Rev. Lett.* **2010**, *105*, 123003–123006. [[CrossRef](#)] [[PubMed](#)]
76. Masuda S.; Rice, S.A. Selective Vibrational Population Transfer using Combined Stimulated Raman Adiabatic Passage and Counter-Diabatic Fields. *J. Phys. Chem. C* **2014**, *119*, 14513–14523. [[CrossRef](#)]
77. Du, Y.-X.; Liang, Z.-T.; Li, Y.-C.; Yue, X.-X.; Lv, Q.-X.; Huang, W.; Chen, X.; Yan, H.; Zhu, S.-L. Experimental realization of stimulated Raman shortcut-to-adiabatic passage with cold atoms. *Nat. Commun.* **2016**, *7*, 12479–12485. [[CrossRef](#)]

78. An, S.L.; del Campo, A.; Kim, K. Experimental realization of stimulated Raman shortcut-to-adiabatic passage with cold atoms. *Nat. Commun.* **2016**, *7*, 12479.
79. Masuda, S.; Nakamura, K. Fast-forward of adiabatic dynamics in quantum mechanics. *Proc. R. Soc. A* **2009**, *466*, 1135–1154. [[CrossRef](#)]
80. Muga, J.G.; Chen, X.; Ruschhaupt, A.; Guéry-Odelin, D. Frictionless dynamics of Bose-Einstein condensates under fast trap variations. *J. Phys. B At. Mol. Opt. Phys.* **2009**, *42*, 241001–241004. [[CrossRef](#)]
81. Schaff, J.-F.; Song, X.-L.; Capuzzi, P.; Vignolo, P.; Labeyrie, G. Shortcut to adiabaticity for an interacting Bose-Einstein condensate. *Europhys. Lett.* **2011**, *93*, 23001–23031. [[CrossRef](#)]
82. Bason, M.G.; Viteau, M.; Malossi, N.; Huillery, P.; Arimondo, E.; Ciampini, D.; Fazio, R.; Giovannetti, V.; Mannella R.; Morsch, O. High-fidelity quantum driving. *Nat. Phys.* **2011**, *8*, 147–152. [[CrossRef](#)]
83. Masuda, S. Acceleration of adiabatic transport of interacting particles and rapid manipulations of a dilute Bose gas in the ground state. *Phys. Rev. A* **2012**, *86*, 063624–063630. [[CrossRef](#)]
84. Torrontegui, E.; Martínez-Garaot, S.; Ruschhaupt, A.; Muga, J.G. Shortcuts to adiabaticity: Fast-forward approach. *Phys. Rev. A* **2012**, *86*, 013601–013606. [[CrossRef](#)]
85. Deffner, S.; Jarzynski, C.; del Campo, A. Classical and Quantum Shortcuts to Adiabaticity for Scale-Invariant Driving. *Phys. Rev. X* **2014**, *4*, 021013–021031. [[CrossRef](#)]
86. Masuda, S.; Nakamura, K.; del Campo, A. High-Fidelity Rapid Ground-State Loading of an Ultracold Gas into an Optical Lattice. *Phys. Rev. Lett.* **2014**, *113*, 063003–063007. [[CrossRef](#)]
87. Ollikainen, T.; Masuda, S.; Möttönen, M.; Nakahara, M. Counterdiabatic vortex pump in spinor Bose-Einstein condensates. *Phys. Rev. A* **2017**, *95*, 013615–013621. [[CrossRef](#)]
88. Ollikainen, T.; Masuda, S.; Möttönen, M.; Nakahara, M. Quantum knots in Bose-Einstein condensates created by counterdiabatic control. *Phys. Rev. A* **2017**, *96*, 063609–063615. [[CrossRef](#)]
89. Unanyan, R.G.; Yatsenko, L.P.; Bergmann, K.; Shore, B.W. Population inversion using laser and quasistatic magnetic field pulses. *Opt. Commun.* **1997**, *139*, 48–54. [[CrossRef](#)]
90. Masuda, S.; Rice, S.A. Fast-Forward Assisted STIRAP. *J. Phys. Chem. A* **2015**, *119*, 3479–3487. [[CrossRef](#)]
91. Chen, X.; Muga, J.G. Engineering of fast population transfer in three-level systems. *Phys. Rev. A* **2012**, *86*, 033405–033410. [[CrossRef](#)]
92. Walls, D.F.; Milburn, G.J. *Quantum Optics*; Springer-Verlag: Berlin/Heidelberg, Germany, 2008.
93. Kuhn, A.; Hennrich, M.; Bondo, T.; Rempe, G. Controlled generation of single photons from a strongly coupled atom-cavity system. *Appl. Phys. B* **1999**, *69*, 373–377. [[CrossRef](#)]
94. Wallraff, A.; Schuster, D.I.; Blais, A.; Frunzio, L.; Huang, R.S.; Majer, J.; Kumar, S.; Girvin, S.M.; Schoelkopf, R.J. Strong coupling of a single photon to a superconducting qubit using circuit quantum electrodynamics. *Nature* **2004**, *431*, 162–167. [[CrossRef](#)] [[PubMed](#)]
95. Sandberg M.; Wilson, C.M.; Persson, F.; Bauch, T.; Johansson, G.; Shumeiko, V.; Duty, T.; Delsing, P. Tuning the field in a microwave resonator faster than the photon lifetime. *Appl. Phys. Lett.* **2008**, *92*, 203501–203504. [[CrossRef](#)]
96. Malinowski, F.K.; Wilson, C.M.; Persson, F.; Bauch, T.; Johansson, G.; Shumeiko, V.; Duty, T.; Delsing, P. Fast spin exchange across a multielectron mediator. *Nat. Commun.* **2019**, *10*, 1196. [[CrossRef](#)]
97. Sigillito, A.J.; Gullans, M.J.; Edge, L.F.; Borselli, M.; Petta, J.R. Coherent transfer of quantum information in a silicon double quantum dot using resonant SWAP gates. *Nature* **2018**, *555*, 633–637. [[CrossRef](#)]
98. Harvey-Collard, P.; Jacobson, N.T.; Bureau-Oxton, C.; Jock, R.M.; Srinivasa, V.; Mounce, A.M.; Ward, D.R.; Anderson, J.M.; Manginell, R.P.; Wendt, J.R.; et al. Spin-orbit Interactions for Singlet-Triplet Qubits in Silicon. *Phys. Rev. Lett.* **2019**, *122*, 217702–217707. [[CrossRef](#)]

